

Topology and Control Innovation for Auxiliary Power Supply in Dimmable LED Drivers

Liang Jia, *Member, IEEE* and Yan-Fei Liu, *Fellow, IEEE*
jialiangleo@gmail.com, yanfei.liu@queensu.ca

Abstract- In this paper, a cost effective architecture based on Flyback topology is proposed for both constant current (CC) output for LED drive and constant voltage (CV) output for AUX supply. A novel nonlinear ramp based control scheme is proposed to decouple the main CC power train from the CV AUX supply and avoid LED output flickering. Small signal modeling is presented to highlight the advantages of this control scheme over conventional peak current mode control. This scheme has been implemented successfully for a 40W dimmable LED driver with a 12V 3W AUX supply.

Keywords: Dimmable LED Drivers, Active Cooling Power Supply, Flyback Converter Modeling, Nonlinear Ramp Control, Small Signal Model

Related work: This paper is an improved version of the work presented in ECCE 2014, entitled “Control Scheme for Decoupling Auxiliary Power Supply in Dimmable LED Drivers”.

Liang Jia is with Consumer Hardware Engineering, Google Inc, Mountain View, CA 94043, USA (e-mail: jialiangleo@gmail.com).

Yan-Fei Liu is with the Department of Electrical and Computer Engineering, Queen’s University, Kingston, ON K7L 3Y4, Canada (e-mail: yanfei.liu@queensu.ca).

I. INTRODUCTION

Due to the rapid transformation of lighting technology, light-emitting diode (LED) becomes the promising light source for the future world and provides: longer lifetime, higher energy efficiency, eco-friendly, better light quality, easier dimming and color control, etc to the consumers. Unlike incandescent light source, LED requires a control gear (usually called LED driver) to provide a constant current (CC) driving current preferably for the best light output performance. As the Internet of Things (IoT) continues to proliferate, connected and smart solutions are influencing more and more areas of our lives, as well as lighting sector. From system point of view, the additional smart features will require separate power and voltage domains from LED load, therefore, integrating an auxiliary (AUX) power supply into LED drivers is an ideal option to facilitate LED luminaire system design and reduce system cost and complexity. This section comprises of a comprehensive overview of the latest trends for indoor dimmable LED drivers, including voltage window, 0-10V dimming controls, and requirements for auxiliary power supplies.

A. Wide Operation Window and Dimming

One major challenge of designing LED driver (often being *ignored* in academic research) is the need of supporting a wide range of output voltage window [1]. The advantage of a wide voltage window driver is very obvious: 1) reduction of cost, number of stock keeping units (SKUs) and logistic complication; 2) reliability enhancement of LED load variation; 3) system design flexibility, etc. An LED driver operation window can be defined using a V-I mapping [2]. In Figure 1, two types of windows are illustrated, A type (red) and B type (blue) [3][4]. In this example, the two types of operation windows have the same V_{LEDmin} and I_{LEDmin} . In both cases, the maximum LED voltage (V_{LEDmax}), minimum LED voltage (V_{LEDmin}), maximum LED current (I_{LEDmax}), minimum LED current (I_{LEDmin}) are defined. In the LED lighting industry, for a high performance LED driver, it often has a 2:1 window of $V_{LEDmax}:V_{LEDmin}$ [3][4]. The LED driver should provide protection for LED over voltage and over current and the levels are called V_{LEDOVP} and I_{LEDOCP} . Usually, the V_{LEDOVP} is 5-10% higher than V_{LEDmax} (only Type B V_{LEDOVP} is shown) and I_{LEDOCP} is defined based on the LED specifications. Also, driver may offer under voltage protection to prevent LED or driver damage during this abnormal condition and the V_{LEDUVP} level is usually 10% lower than the nominal V_{LEDmin} .

In both windows, the LED practical operating window is drawn in solid-line boxes. The slope of $\frac{\Delta V_F}{\Delta I_F}$ in the LED practical operating window is determined by the LED dynamic resistance [6][7][8][9]. In type A window, it is worth noticing that due to the LED dynamic resistance, a portion of the driver operation window cannot be practically used (for example, the red * operating point in the window). For a reliable design, the driver should be able to operate properly and meet all the design specifications at the corner of $V_{LEDmax} * I_{LEDmax}$, i. e. P_{max} . In order to extend the window for a same power capability, type B is introduced for alternative. The constant power line is defined for a power of $V_{LED} * I_{LED} = P_{max}$. In this way both the V_{LEDmax} (B) and I_{LEDmax} (B) can be extended from the A type window. And the practical LED load operation window is thus extended significantly. B type window utilizes the power capability of the LED driver more efficiently.

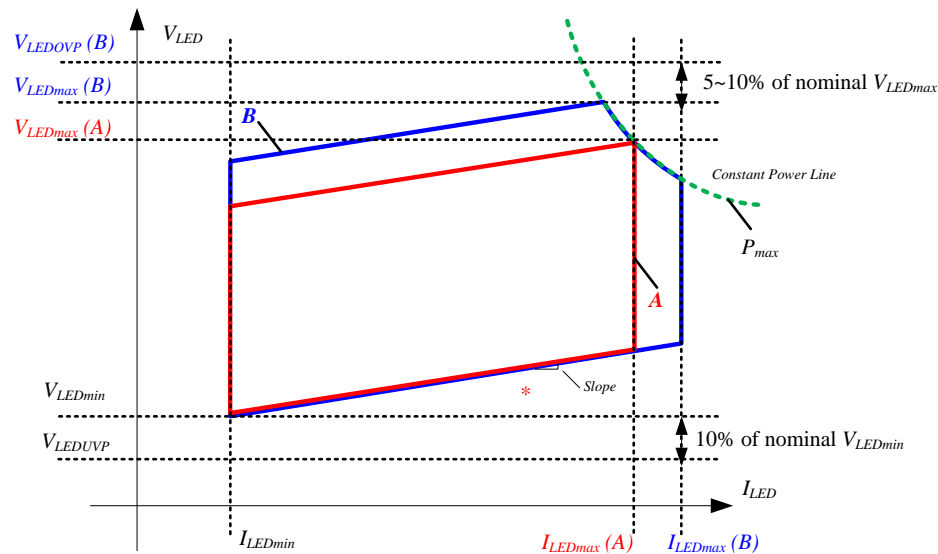


Figure 1 LED driver operation window: A and B types

Dimming control becomes very common for LED lighting application due to the simplicity of controlling light output by driving current [10]-[12]. A commonly used low voltage dimming interface for indoor lighting is 0-10V dimming interface. There are many different names of this interface, for example, Mark 7 dimming (first introduced by Philips in North America), 1-10V dimming (in Europe), etc. And it was firstly introduced for dimmable fluorescent lighting system and adapted later into HID and LED-based lighting (both indoor and outdoor applications). The 0-10V dimmer can be simply designed as a variable resistor and the ballast/driver has to provide a

power source to generate a voltage potential between the two dimming leads (usually violet as positive, and grey as negative).

To sum up, for industrial LED applications, the LED driver has to support a wide range of LED load voltage and current, especially in dimmable applications.

B. Auxiliary Power Supply

Even though high-brightness LEDs (HBLEDs) are rapidly advancing in terms of energy efficiency, heat remains the nemesis of most HBLED illumination systems as shown in Table 1 generated by non-radiated recombination of electrons and holes in the HBLED semiconductor material. Although LEDs have the advantage of producing light in a narrow, well-defined wavelength, this also limits the devices' ability to radiate excess heat in the form of infrared energy [13][14], therefore, still around 60-75% of the LED power remains as heat [2][15].

Table 1 Heat and energy distribution of various white light sources

	White HB LED	Fluorescent	HID (Metal Halide)	60W Incandescent
Visible Light	25-40%	21%	27%	8%
Infrared	~0%	37%	17%	73%
UV	0%	~0%	19%	0%
Total Radiant Energy	25-40%	58%	63%	81%
Remaining Heat	60-75%	42%	37%	19%

Other than increase the heat sinking capacity in the LED luminaire, a growing number of indoor LED lighting applications will require forced-air convection because of the high intensity of light needed such as recessed light, spot light and track light. Regular fans, however, introduce life time and reliability concern and for indoor application the undesirable motor noise is also a disadvantage. A novel cooling solution is called SynJet cooler [14][16]. These small coolers use an electromagnetically-coupled diaphragm to pulse high-velocity jets of air through nozzles. As the air is forced out of the nozzle, a vortex is created. Once the vortex flow propagates downstream from the nozzle, it entrains the surrounding air [16]. The cooler requires 12V DC power supply to provide DC+AC current.

Also, due to the downward-trending prices and limited price competition opportunities in “conventional” LED lighting, the ability to provide new value-added features, such as connectivity,

enables additional growth potentials. Therefore, a deeper transition towards smart solutions becomes a natural direction for the entire LED lighting industry [5]. The idea that lighting can now communicate (via wireless network) and interact with the environment (via various sensors) and the people or things around it, is opening up a new requirement for power delivery in the system to supply the added features. 12V DC is a general voltage level to support multiple digital and analog voltage domains (5V, 3.3V, etc) just like in computing application.

So from system point of view, a preferred low-medium power indoor LED driver architecture should offer a built-in auxiliary power supply for cooling or digital control/communication devices. A lot of research has been conducted for single stage Flyback LED driver with PFC for low power application, however, the high output ripple at low frequency is not favorable for high performance dimmable indoor application [17]-[23]. In [24]-[27], several methods have been discussed to reduce or cancel the low frequency ripple. Boost PFC+Flyback topology is a low cost and good candidate for low-medium power LED application ($25W < P_{out} < 50W$). But it is very challenging to create a sufficient constant voltage (CV) auxiliary supply ($P_{aux} > 2W$) directly from conventional Flyback topology for dimmable LED lighting application.

So, in this paper, a novel power architecture and control scheme is proposed to offer a decoupled CV power supply for the purposes of active cooling, lighting control, sensing, etc from the same power converter, which outputs CC to the LEDs. In section II, existing techniques and issues are introduced for research background. In section III, the control scheme is outlined and the proposed scheme generates a nonlinear ramp to decouple the CV output from CC output and prevents from light flickering during fan operations in LED dimming condition. In section IV, the operation and implementation of the proposed control scheme is explained in details. The implementation of the controller can be based on commonly used peak current mode (PCM) controller and no additional silicon development is required. In section V, small signal model is built to analyze the advantages of the propose controller. Experimental results verify the benefits of this proposed LED driver architecture and control scheme in a 40W 700mA 0-10V dimmable LED driver in section VI. Finally, conclusion is drawn in the end of the paper. Appendix is also provided for detailed derivation for some of the critical design equations in the paper.

A version of this paper was presented at the ECCE 2014 conference [1]. The paper has been extended and improved, and derivation of critical design equations has been added.

II. EXISTING TECHNIQUES AND ISSUES

In order to better illustrate the significance of the proposed technology, a detailed review of the existing techniques to create CV auxiliary supply is provided in this section.

There is a possibility of using auxiliary winding in the Boost PFC inductor to create an auxiliary power supply, however, 1) with peak detector output (diode rectifier and output capacitor) from either a flyback or forward winding, the rectified AC line voltage will be reflected to the auxiliary output, resulting in large voltage variation; and 2) with charge pump supply, the variation may also occur at line voltage zero crossing moment, due to higher current draw to support the constant auxiliary power. And oversized charge pump supply will require output voltage clamp to prevent from over voltage event at no load and very light load condition at the auxiliary output, resulting in unnecessary power losses. More importantly, in both cases, the commonly used peak current mode controlled Boost PFC performance will be degraded, especially at line voltage zero crossing, when higher auxiliary current is reflected and added on top of the sensed Boost inductor current. Therefore, in this paper, the input AC rectifier and Boost PFC stage is ignored for simplicity and the input to the Flyback converter will be a well-regulated DC bus voltage.

The first solution is shown in Figure 2, and a multi-output Flyback converter is used to generate the auxiliary supply. The flyback voltage V_{fb} is roughly proportional to the output voltage V_{out} . However, as outlined in section I, for a wide window LED driver (for example, $V_{LEDmax}:V_{LEDmin}=3:1$), the variation of flyback voltage V_{fb} (the input of the auxiliary power supply) is 3:1 roughly. If non-ideal transformer coupling is considered for different LED driving current scenarios, the voltage variation from the flyback winding will be much larger. Therefore, flyback winding is not suitable to provide a constant input level V_{fb} for the AUX supply. Otherwise, it requires a Buck-Boost stage to deal with the wide input range of V_{fb} . For example, if the designer selects $V_{fbmin}>12V$ at minimum number of LEDs to design the 12V AUX supply using Buck converter, then at maximum number of LEDs, the V_{fbmax} will be larger than 36V, efficiency will be compromised and power component cost will be increased to handle higher voltage stress.

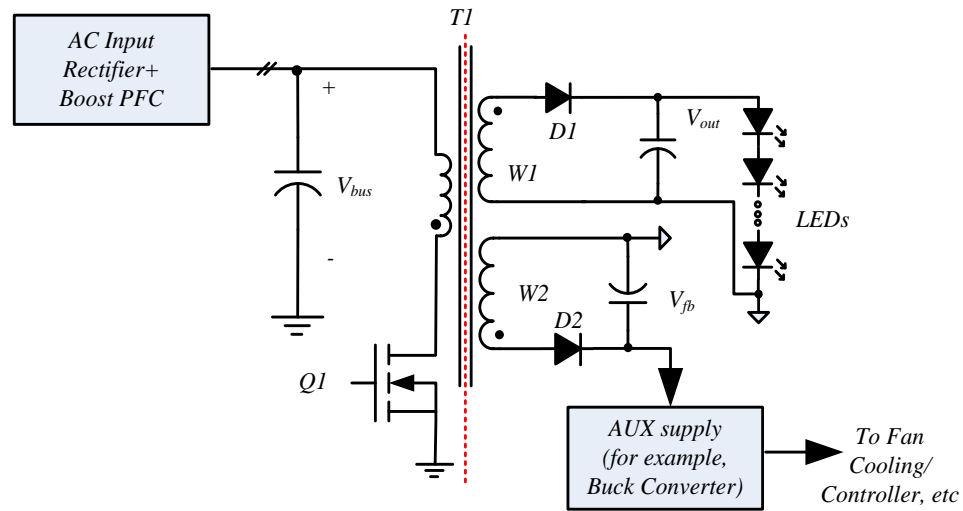


Figure 2 AUX supply from a Flyback winding

The second method is shown in Figure 3. An additional Buck converter stage is powered directly from the LED main output. Other than the aforementioned range of V_{out} for AUX supply input, the operation of AUX supply will interrupt the main power train, resulting in LED output flickering or other light quality degradations. Expensive switcher IC/bulky configuration will be required for designing the Buck stage with $>60V_{max}$ input.

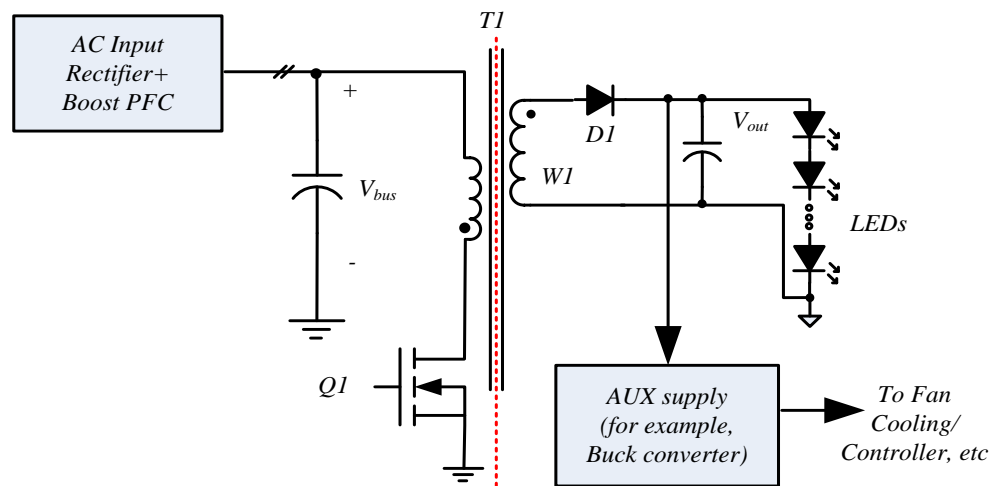


Figure 3 AUX supply from main LED output

The third method as shown in Figure 4 is to use a separate Flyback converter powered from the high voltage DC bus for CV AUX supply. This configuration is used in some design that requires isolated standby power supply. During the standby mode, the main power train MOSFET Q1 will be off all the time, as well as the PFC stage. The V_{bus} will be the rectified line voltage filtered by

V_{bus} capacitor and FET Q2 is controlled to regulate the AUX output voltage. However, in LED lighting application for thermal management purposes, the fan will only need to be operated when the LED light output power is high and additional heat dissipation is required. So for the auxiliary supply, the standby mode is not applicable. Although using this option, the AUX supply load is also completely independent from the main LED power train, the design will be bulky and more expensive, because of the extra high voltage switch/switcher IC [28], isolation transformer, etc.

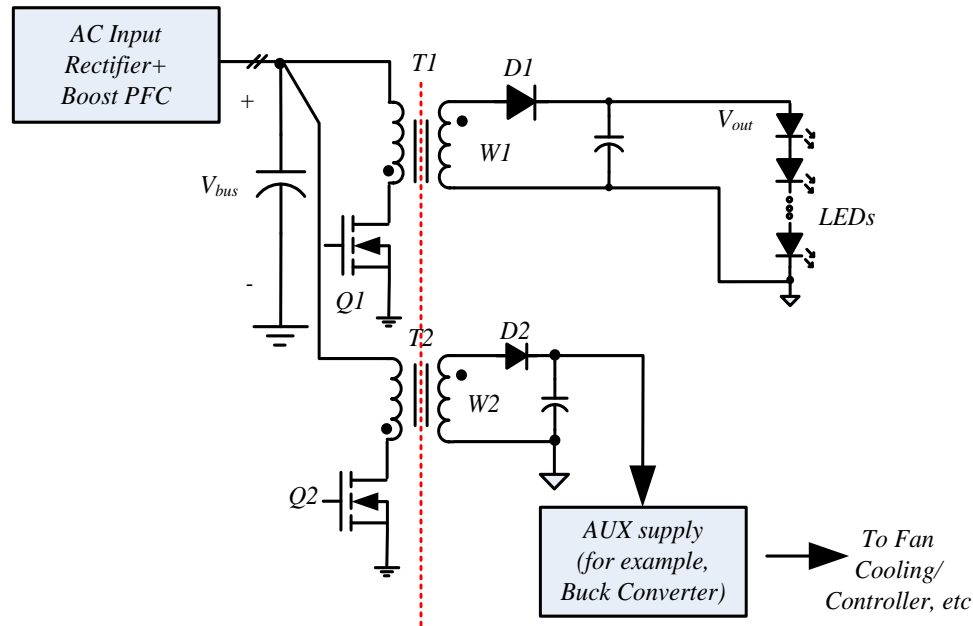


Figure 4 AUX supply from a dedicated Flyback converter

Another option is shown in Figure 5, where a forward winding is used to provide a relatively constant DC voltage V_{fw} (about 20V) from the DC bus and a Buck converter to step down this DC voltage for 12V AUX supply. A cost effective and commonly available switcher IC can be used for this AUX supply [31]. However, using conventional peak current mode control (PCMC), when the LED string is dimmed by dimmer, the AUX load starts affecting the main power train more severely and causing visible flicker at the LED output. This issue will be analyzed in more details in the next section.

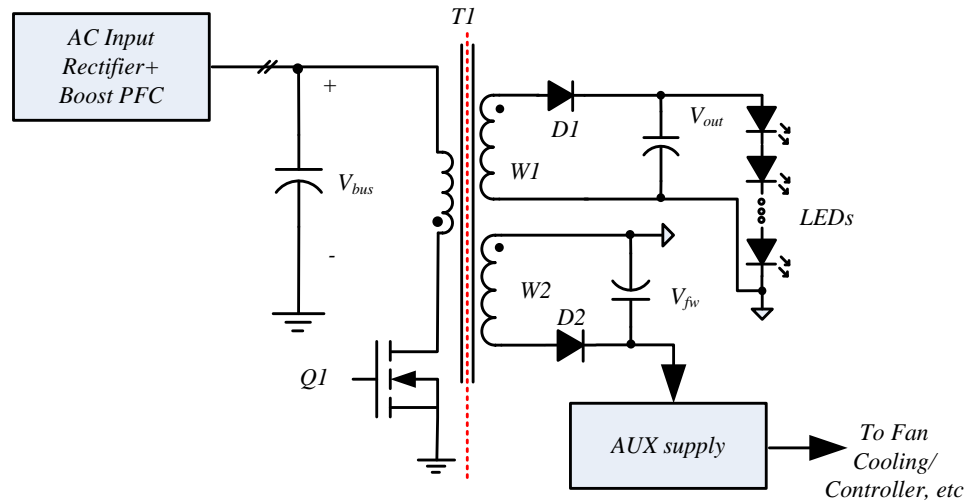


Figure 5 AUX supply from a forward winding

This section provides a detailed review of the existing technology for generating a CV auxiliary power supply, including flyback winding supply, main output converter, dedicated Flyback converter and a forward winding supply. The issue of each of the methods is also outlined.

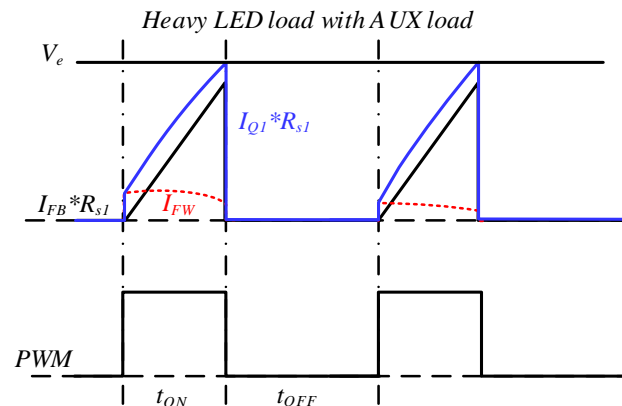
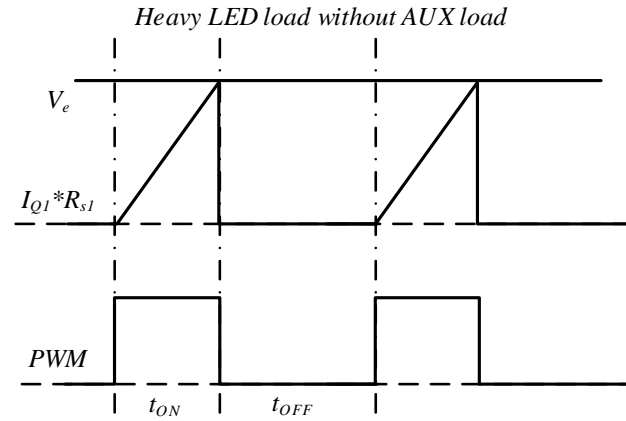
III. PROPOSED DECOUPLING METHODS

To resolve the issues discussed in the previous section, a new control scheme is presented in this section to decouple the AUX supply from the main LED driving power train.

The forward winding offers a relatively constant output voltage with fixed ratio to the DC bus voltage. This makes forward winding a promising option for this CV AUX application with lower cost and system complexity. At 40W power level, where conduction loss is not yet dominant, BCM Flyback offers such benefits as smaller size of the magnetics (lower inductance) [29], higher efficiency (lower switching loss on the main FET with nearly voltage valley switching and zero current switching; lower output rectifier reverse recovery loss), etc, compared with CCM mode or fixed frequency Flyback with conventional voltage mode duty cycle control. Also, loop compensation will be more complicated due to the relatively lower frequency RHP zero in CCM Flyback converter [30]. So in this paper, the conventional peak current mode control (PCMC) is selected and used for Flyback converter control as illustrated in Figure 6. In the case shown in Figure 6 (A), Flyback stage is operating without the AUX supply in BCM. V_e signal is the output from the error amplifier (EA). And the main FET Q1 sensing signal is $I_{Q1} * R_{sense}$ and as soon as the equation (1) is satisfied, Q1 will be turned off. Q1 turns back on again when the magnetizing current of T1 goes to zero.

$$V_e = I_{Q1} \cdot R_{sense} \quad (1)$$

However, once the forward winding is employed for the CV AUX, it is noted that the current reflected from forward winding I_{FW} will be also added to the main FET drain current I_{Q1} during t_{ON} . I_{FW} is varying with the AUX load demanding, V_{bus} low frequency ripple, V_o , etc. The triangular shape of the sensing signal $I_{Q1} \cdot R_{sense}$ is thus distorted. At full power or heavy LED load condition when $P_{out} \gg P_{aux}$, flyback winding current I_{FB} is still dominant as shown in Figure 6. (B). But at LED dimming condition, the variant reflected forward winding current I_{FW} will start to dominate the I_{Q1peak} shown in Figure 6. (C) and the on time t_{ON} will vary a lot cycle by cycle, resulting in system instability and LED output random flickering.



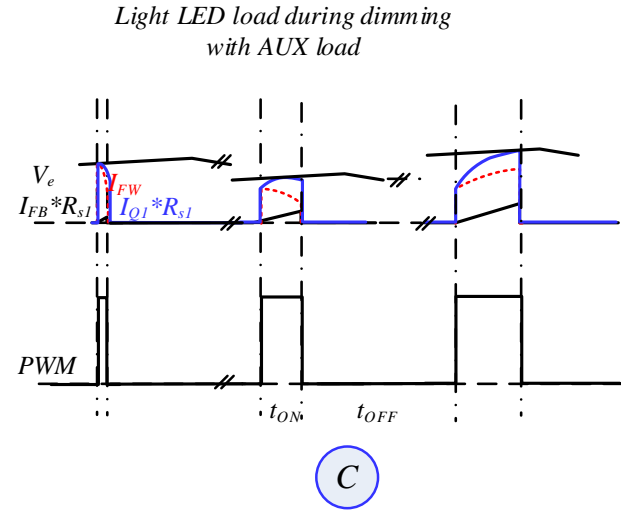


Figure 6 Conventional peak current mode control

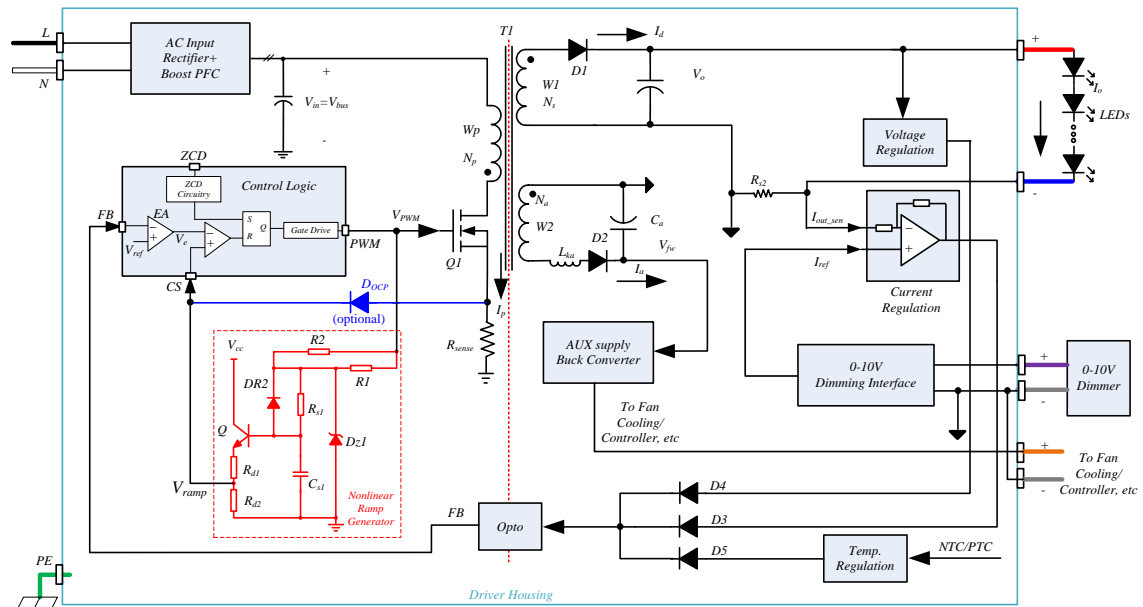


Figure 7 Proposed system, functional blocks and LED driver connection

Therefore, in order to take full advantage of the power architecture shown in Figure 5, a novel control scheme is proposed to offer a decoupled CV auxiliary power supply for the purposes of active cooling, lighting control, sensing, etc from the same power converter, which delivers CC to the LEDs. Proposed system and functional blocks are shown in Figure 7. The 0-10V dimmer is connected to the LED driver using the violet (positive) and grey (negative) wires and the dimmer circuit is shown in Figure 23. The LED driver internal 0-10V dimming interface block will 1) provide bias current to the 0-10V dimmer (150μA for example) and create a DC voltage (0-10V in this

case, according to the dimmer position) between violet and grey wires; and 2) read this *DC voltage* and translate it into I_{ref} for setting the output current reference in the current regulation loop. Different from the linear ramp signal from the sensed I_{Q1} , the control scheme generates a nonlinear ramp (highlighted in red in Figure 7) to 1) decouple the CV output from CC output and prevents from light flickering during fan or other auxiliary load operations; 2) improve noise immunity of the controller at dimming condition; 3) reduce the variation of the system loop response at different operating conditions for easier compensation design and 4) offer optional redundant over current and over power protection. The ramp signal V_{ramp} is generated (from the PWM gate signal of the main FET Q1) to substitute the current sensing signal $I_{Q1} * R_{sense}$ in the control scheme, as shown in Figure 8 (A), (B) and (C). This V_{ramp} signal will then compare with V_e to turn off the FET in each switching cycle. The function of V_{ramp} is predefined to modulate t_{ON} based only on LED output regulation feedback loop (i. e. V_e signal), so V_{ramp} is not influenced by I_{FW} anymore. Detailed design guidelines will be provided in the next sections.

For example, in Figure 7, when higher LED output current is desired, the current reference signal I_{ref} will be increased on the secondary side. And the secondary side error amplifier will compensate the LED output current. Through the closed feedback loop control, V_e will be increased to V_e' . V_{ramp}' thus follows to reach V_e' and finally extends t_{ON}' for larger LED output current in Figure 8 (A) (in dashed green). In another case, when LED current is under steady state, if AUX load is increased, t_{ON} will not be changed because of the unchanged I_{ref} and V_e , but I_{FW}' will be higher during t_{ON}' to provide more power for AUX load in Figure 8 (B) (in dashed red).

Besides the coupling impact, the instability at full *dimming* condition can be also caused by the very low sensing signal ($I_{Q1} * R_{sense}$) level (at around 10mV using conventional current mode control scheme), which is very sensitive to board noise (caused by $\frac{dv}{dt}$ and $\frac{di}{dt}$). So a nonlinear type of ramp signal is proposed and shown in Figure 9, which has higher slew rate at the beginning of the charging process and then slows down until it reaches the V_e level.

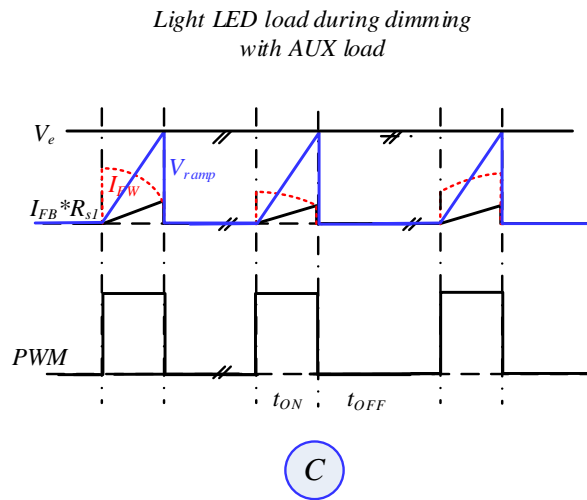
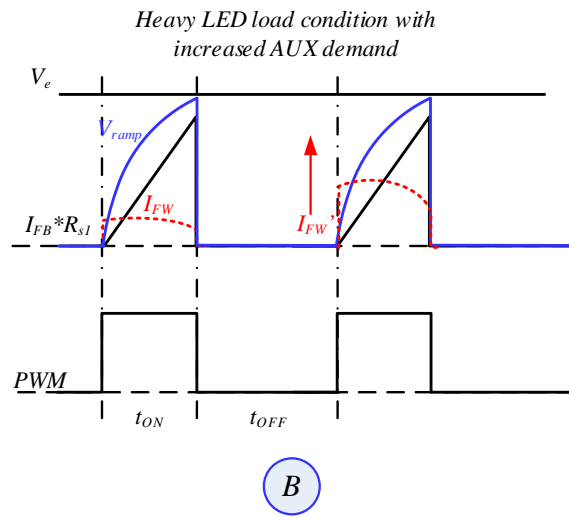
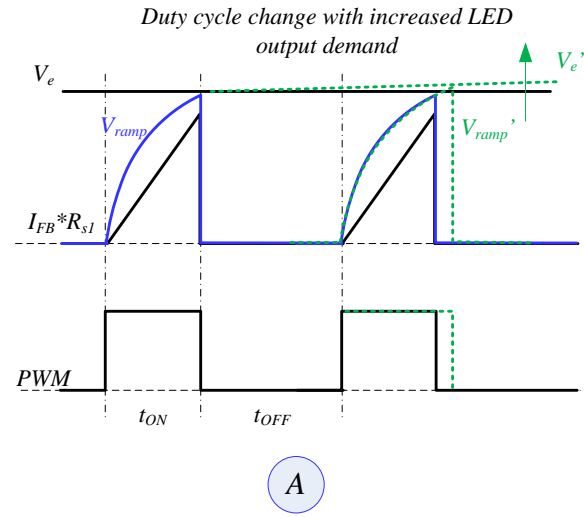


Figure 8 Proposed nonlinear ramp control scheme

For a typical application at this power level, the FET turn-on time t_{ON} is usually around hundreds of nano-seconds (t_{ONmin}) to several micro-seconds (t_{ONmax}). A proper time constant of $\tau=R_{sI}C_{sI}$ is selected accordingly, where $t_{ONmin}<\tau<t_{ONmax}$. In this way, at the beginning of the charging process, the V_{ramp} signal rises faster to get at least about 200mV signal at full *dimming* condition (V_{ramp2} in Figure 9). Compared with 10mV level with conventional peak current mode control, this is one order improvement for better noise immunity. Also, in the next section, it will be shown that the nonlinear ramp actually reduces the system gain at dimming condition. At heavy LED load condition, a higher V_{ramp} will be generated but V_{ramp} must be lower than over-current-protection (OCP) threshold to guarantee no OCP will be triggered in the Flyback stage. So, this scheme utilizes the saturated top of the nonlinear ramp in Figure 8 to extend the output power capacity. This is the second benefit to use nonlinear ramp.

In many indoor LED lighting applications, where LED voltage is $<60V$, the LED driver may be certified for UL Class 2 safety power units [32] and highly simplify the lighting fixture isolation design, resulting in lower system implementation cost as well. However, the UL Class 2 standard requires additional hardware and/or software redundancy in case of single-fault failure in the system to guarantee the safe output voltage and power. By adding a diode D_{OCP} to the existing current sense signal (in Figure 7), there will be redundant OCP/over power protection (OPP), in case of one implementation of the protection function is failed. For example, if the R_{sense} is shorted in a fault condition, the nonlinear ramp will still be able to fulfill the protection. During normal condition, the D_{OCP} will be reverse biased and will not impact the control scheme.

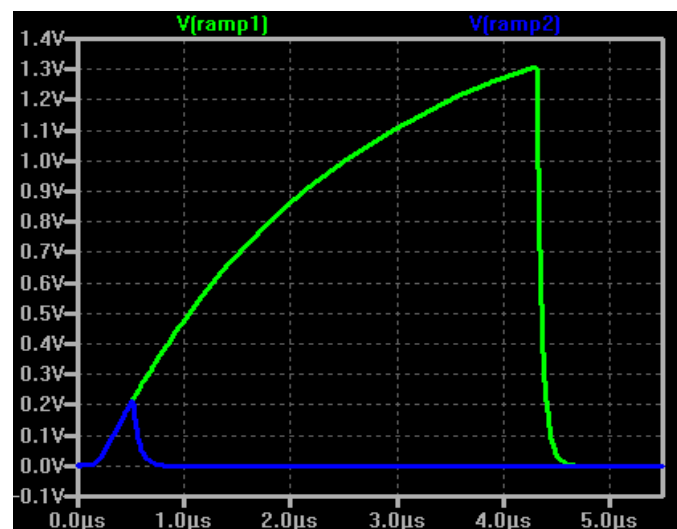


Figure 9 Simulated nonlinear ramp signal (Green: ramp level at t_{ONmax} ; Blue: ramp level at t_{ONmin})

IV. BASIC OPERATIONS AND SYSTEM IMPLEMENTATION

The system implementation diagram is shown previously in Figure 7. The AUX supply is powered from forward winding W2 and D2. AUX supply block is typically a step down *DC-DC* switcher (for example, ST 5970D [31]) to create 12Vdc, 250mA_{max} supply. The input of the ramp generator is the gate signal from the gate control logic IC. The output of the ramp generator is called V_{ramp} , which simulates the signal of $I_{Q1} * R_{sense}$. The real current sensing signal ($=I_{Q1} * R_{sense}$) is used for redundant OCP and OPP only. The gate control logic will compensate the loop according to the FB signal from secondary side (using built-in EA, the output of EA is called V_e) and turn off Q1 as soon as the $V_{ramp} > V_e$. On the secondary side, the current regulation loop passes the feedback signal *FB* to the primary side across the isolation barrier through the optocoupler.

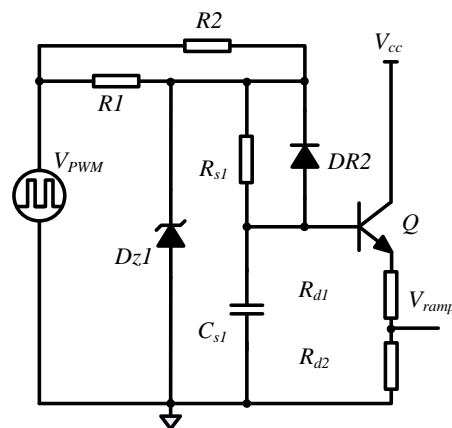


Figure 10 Analog ramp generator

In Figure 10, an analog circuit implementation of the ramp generator is shown. V_{PWM} is the gate signal from the gate control logic IC. $R1$ and $Dz1$ clamp the signal to a square waveform ($V_{high} = V_{gd}$). R_{S1} and C_{S1} form a RC time constant τ and the square waveform will be filtered to generate the ramp signal. When the gate signal V_{PWM} is at about 0V, $R2$ and $DR2$ will help to quickly discharge C_{S1} to about 0.6V. In order to compensate the diode forward voltage drop of $DR2$ and increase loading capability, a bipolar emitter follower Q stage is used to condition the signal. R_{d1} and R_{d2} form a voltage divider for proper V_{ramp} signal level.

To properly design the nonlinear ramp generator circuit, the design rules are provided in equations (2)-(5). Based on the Flyback converter principles, the maximum turn-on time t_{ONmax} can be calculated using equation (2). Please refer to Appendix A for more details for derivation.

$$t_{ON\max} = \frac{-\beta + \sqrt{\beta^2 - 4\alpha\gamma}}{2\alpha} \quad (2)$$

And the parameter α , β and γ can be calculated in equations (3)-(5). $V_{in\min}$ is the minimum input DC voltage (425V in this case) to the Flyback stage, in this case is the DC bus voltage. L_m is the primary magnetizing inductance of the transformer. C_{tot} is the total equivalent output capacitance of the MOSFET. $V_{o\max}$ is the maximum output voltage of the Flyback converter. $P_{o\max}$ is the maximum output power. V_F is the forward voltage of the output rectifier diode. η is the efficiency of Flyback power stage. Please refer to Appendix A for more details for derivation.

$$\alpha = \frac{1}{2} \frac{V_{in\min}^2}{L_m} \quad (3)$$

$$\beta = -\frac{P_{o\max}}{\eta} \left(\frac{V_{in\min}}{n(V_{o\max} + V_F)} + 1 \right) \quad (4)$$

$$\gamma = -\frac{P_{o\max}}{\eta} \left(\pi \sqrt{L_m C_{tot}} \right) \quad (5)$$

Based on the calculation, the maximum t_{ON} at different operating points is shown in Figure 11. At maximum power (700mA and 60V), t_{ON} is about 4.5 μ s and at minimum power (70mA and 20V), t_{ON} is about 500ns. And the results match the simulation closely shown in Figure 9. In the experimental results section, it will demonstrate that the calculated results also match the experiments very well.

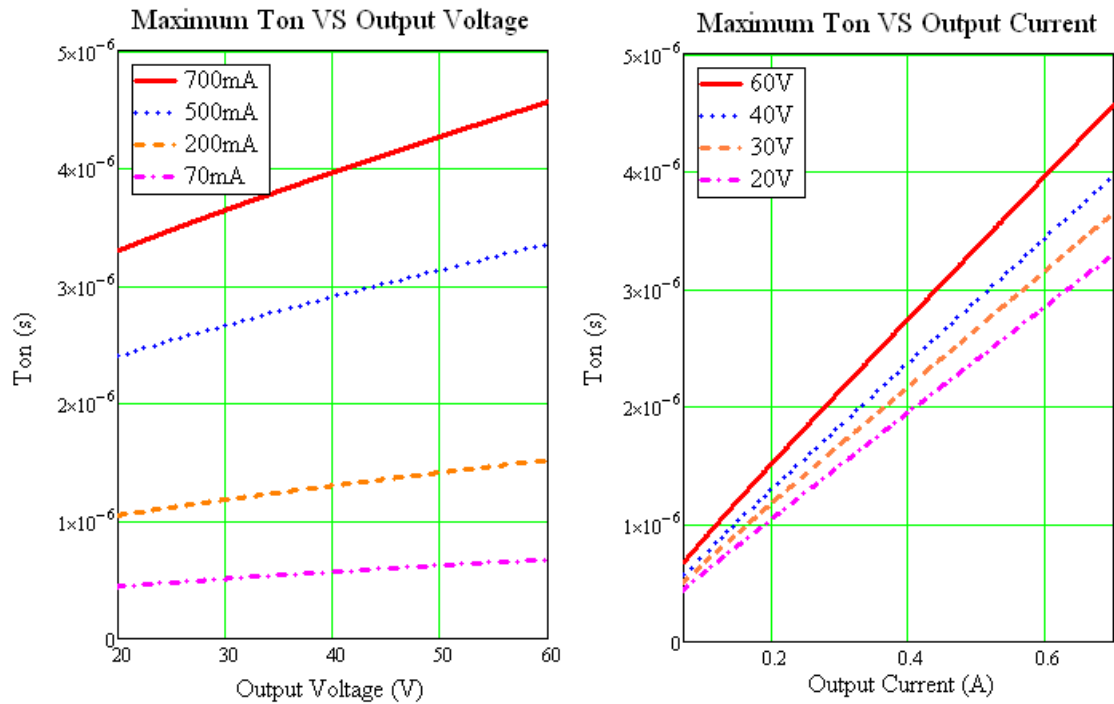


Figure 11 Maximum t_{ON} time at different operating conditions at $V_{inmin}=425V$

Finally, we need to make sure the voltage V_{ramp} in equation (6) to the gate control logic is less than the over current protection threshold level. In this way, we can tune the R_{S1} and C_{S1} to achieve maximum output power. In Figure 12, the equivalent circuit of the ramp generator is shown. When the gate is off, the voltage of C_{S1} is clamped to the diode voltage V_{F_DR2} after the discharging of C_{S1} through $R2$. And the ramp voltage V_{ramp} at this moment will be roughly 0V, due to the compensation between V_{be} of Q and V_{F_DR2} . When the gate drive voltage is high, the capacitor C_{S1} voltage will be charged up and the voltage of the ramp can be calculated in equation (6). V_{be} is the base-emitter voltage of Q and V_{F_DR2} is the forward voltage drop of $DR2$ in Figure 10. V_{gd} is the clamping voltage of $Dz1$. It is noted that in equation (6), there are actually two design parameters: 1) the time constant $\tau=R_{S1} C_{S1}$ and 2) the divider ratio $\frac{R_{d2}}{R_{d1}+R_{d2}}$. So based on the desired peak ramp voltage levels for t_{onmin} and t_{onmax} , the designer can solve these two parameters simply and flexibly.

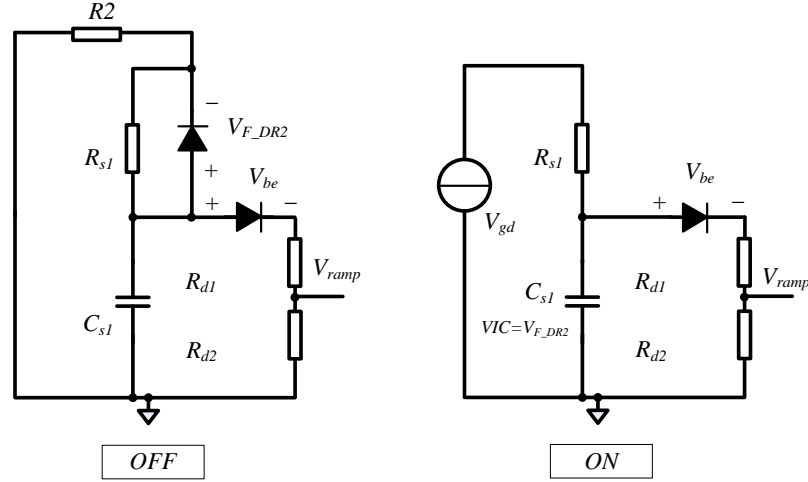


Figure 12 Equivalent circuit for the ramp generator during ON and OFF modes

$$V_{ramp} = \left[V_{F_DR2} + V_{gd} \left(1 - e^{-\frac{t_{ON_max}}{R_{s1} \cdot C_{s1}}} \right) - V_{be} \right] \left(\frac{R_{d2}}{R_{d1} + R_{d2}} \right) \quad (6)$$

The relationship between control signal V_{ramp} and LED current I_o is plotted in Figure 13. For example, when the LED load voltage is 60V and current is 700mA, the V_{ramp} peak value is about 1.3V. While the LED load voltage is 20V and current is 70mA, the V_{ramp} peak level is around 200mV. This result matches the simulation in Figure 9 also very well.

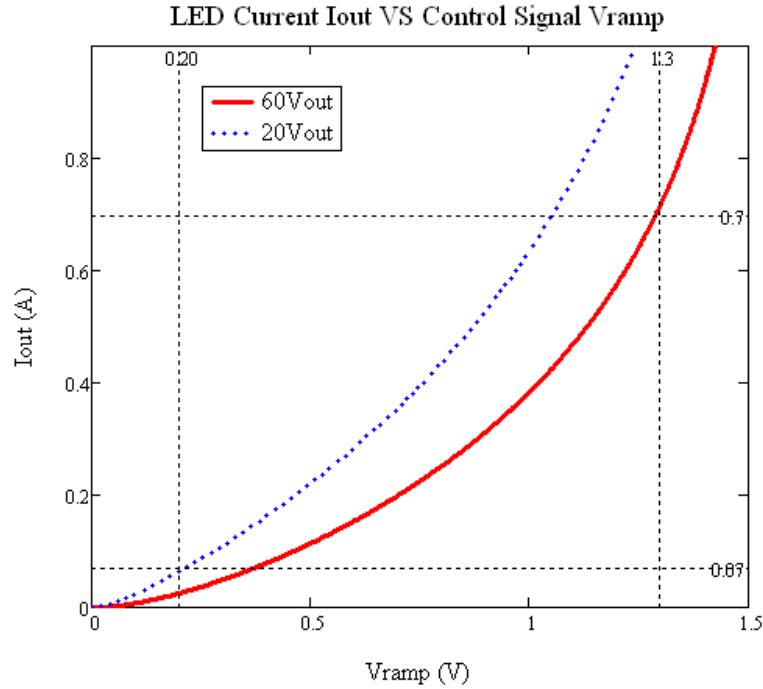


Figure 13 LED current I_o VS control signal V_{ramp} at $V_{imin}=425V$

V. SMALL SIGNAL MODELING

In this section, the small signal model is derived to provide the insight of the coupling issue between CC and CV outputs using PCM control and the benefits of the proposed method.

Flyback converter can be analyzed with a Buck Boost equivalent model shown in Figure 14 (left side). In the practical implementation, the leakage inductance of the Flyback transformer can be controlled lower than 1% of the magnetizing inductance, therefore, in the model, the leakage inductance is ignored. And the average large-signal model of a peak current controlled Flyback converter (in BCM) can be obtained by replacing the semiconductors Q1 and D1 in Figure 14 (left side) with dependent current sources I_{ac} and I_{pc} [33]-[40]. I_{ac} is the average current of the MOSFET Q1 and I_{pc} is the average current of the diode D1 over a switching cycle.

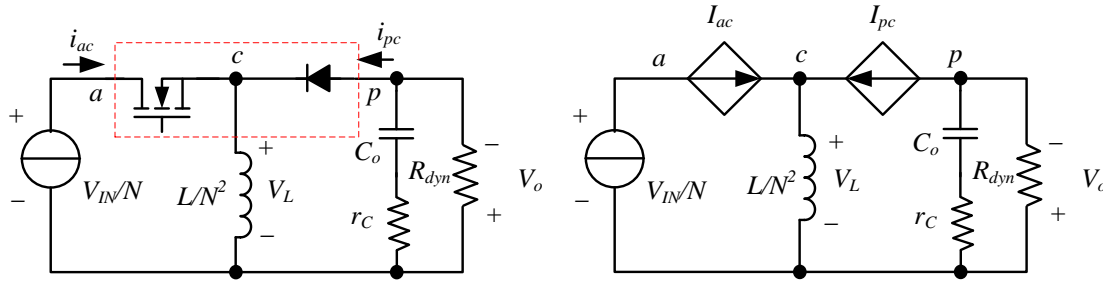


Figure 14 Equivalent Buck Boost Model for Flyback converter and average large signal model

When the AUX supply is loaded and Q1 is on (shown in Figure 7), the current flows through the diode D2 is near-constant and continuous due to winding leakage inductor L_{ka} and output filter capacitor C_a . It is assumed that the average AUX load current is I_a . The average output diode current I_d can be calculated in equation (7), where V_F is the forward voltage of D1, V_o is the output voltage, V_{in} is the bus voltage, $n = \frac{N_p}{N_s}$, and $n_a = \frac{N_p}{N_a}$. Please refer to Appendix B for more details for derivation of equation (7), using PCM control.

$$I_d(V_{in}, V_o, V_e, I_a) = \left(\frac{n \cdot V_e}{2R_{sense}} - \frac{I_a \cdot [V_{in} + n(V_o + V_F)]}{2n_a \cdot (V_o + V_F)} \right) \frac{V_{in}}{V_{in} + n(V_o + V_F)} \quad (7)$$

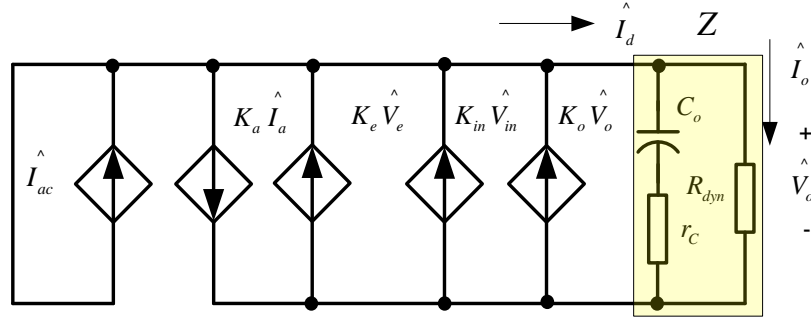


Figure 15 Small Signal Model

The small signal model can be obtained by setting all DC source values to zero (in Figure 15). Then I_d is linearized around its steady state operating point in (2), where $K_e = \frac{\partial I_d}{\partial V_e}$, $K_{in} = \frac{\partial I_d}{\partial V_{in}}$, $K_o = \frac{\partial I_d}{\partial V_o}$ and $K_a = \frac{\partial I_d}{\partial I_a}$. The equations of K_e , K_{in} , and K_o for a Flyback converter without AUX load (i.e. $I_a=0$) are presented in (9)-(11). It is noticed that in the small signal model in equation (8), there is a coupling gain $-K_a$ path from \hat{I}_a to \hat{I}_d , where K_a can be calculated in equation (12), resulting in LED output flickering, while auxiliary loading is varying.

$$\hat{I}_d = K_e \hat{V}_e + K_{in} \hat{V}_{in} + K_o \hat{V}_o - K_a \hat{I}_a \quad (8)$$

$$K_e = \frac{nV_{in}}{V_{in} + n(V_o + V_F)} \frac{1}{2R_{sense}} \quad (9)$$

$$K_{in} = \frac{nV_e}{2R_{sense}} \frac{n(V_o + V_F)}{[V_{in} + n(V_o + V_F)]^2} \quad (10)$$

$$K_o = -\frac{n^2V_e}{2R_{sense}} \frac{V_{in}}{[V_{in} + n(V_o + V_F)]^2} \quad (11)$$

$$K_a = \frac{V_{in}}{2 \cdot n_a (V_o + V_F)} \quad (12)$$

The transfer function from error voltage \hat{V}_e to output current \hat{I}_o is obtained in equation (13), where Z is the output impedance in equation (14) and R_{dyn} is the LED dynamic resistance [8].

$$G_{ie} = \left. \frac{\hat{I}_o}{\hat{V}_e} \right|_{\hat{V}_m=0} = \frac{Z \cdot K_e}{R_{dyn} \cdot (1 - Z \cdot K_o)} \quad (13)$$

$$Z = \frac{R_{dyn} (1 + s \cdot C_o \cdot r_C)}{1 + s \cdot C_o \cdot (r_C + R_{dyn})} \quad (14)$$

Bode plot of G_{ie} for conventional peak current mode control is shown in Figure 16. When the Flyback stage is operating at $V_{LEDmin}=20V$, the DC gain is higher and zero location is at higher frequency, compared with $V_{LEDmax}=60V$ (shown in Figure 16) for the same output current. This explains that using the same compensator, Flyback LED driver stage is less stable when powering less number of LEDs.

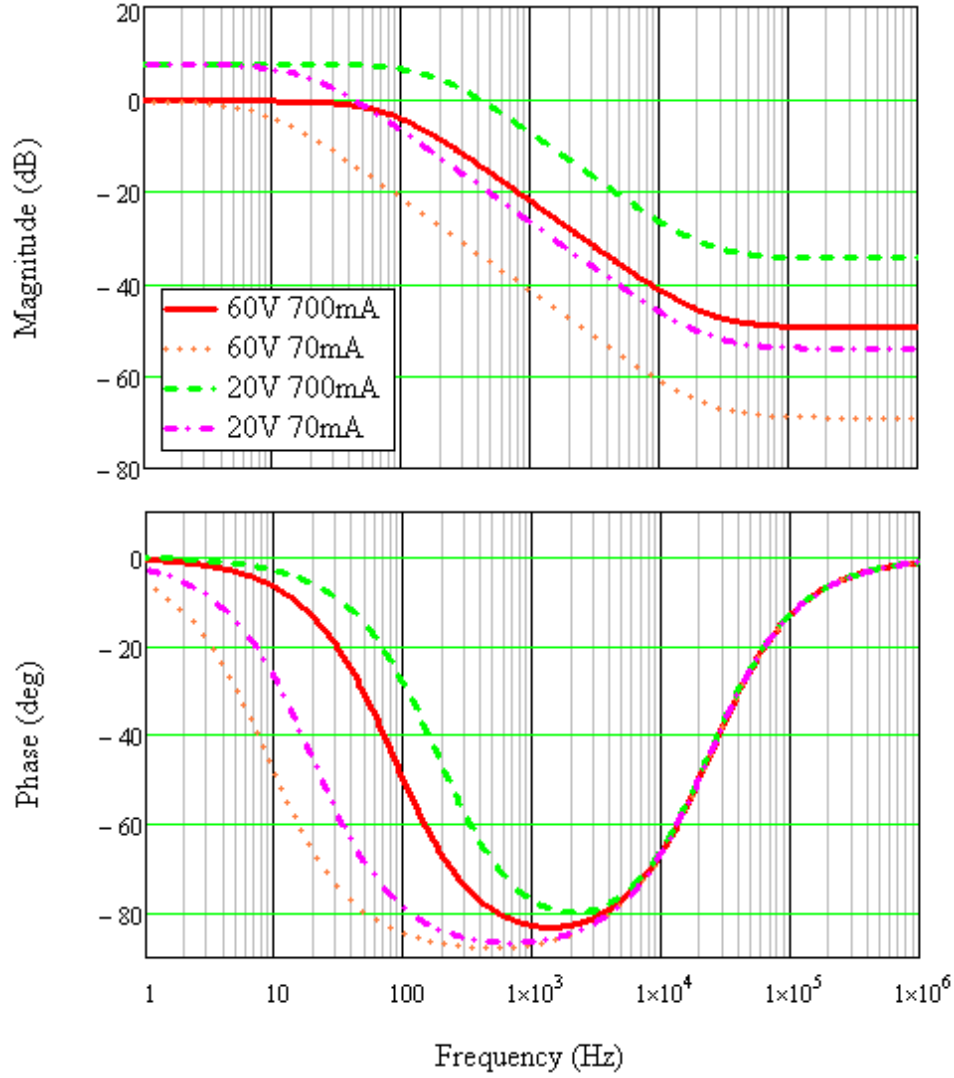


Figure 16 Bode plot of G_{ie} for conventional peak current mode control

Using the same modeling principles, the average diode current I_d of Flyback stage controlled by the proposed nonlinear ramp control scheme can be calculated as equation (15), where t_{ON} can be obtained in equation (16). Please refer to Appendix C for more details for derivation.

$$I_d(V_{in}, V_o, V_e) = \frac{nV_{in}^2}{2L_m \cdot \left[V_{in} + n(V_o + V_F) + \frac{TR \cdot n(V_o + V_F)}{t_{ON}} \right]} \cdot t_{ON} \quad (15)$$

$$t_{ON} = -R_{s1} C_{s1} \ln \left(1 - \frac{V_e}{V_{gd}} \frac{R_{d1} + R_{d2}}{R_{d2}} \right) \quad (16)$$

The small signal model can be derived using the equation in (17), where $K_e' = \frac{\partial I_d}{\partial V_e}$, $K_{in}' = \frac{\partial I_d}{\partial V_{in}}$, and $K_o' = \frac{\partial I_d}{\partial V_o}$. The equations of K_e' , K_{in}' , and K_o' are represented in (18)-(20).

$$\hat{I}_d = K_e' \hat{V}_e + K_{in}' \hat{V}_{in} + K_o' \hat{V}_o \quad (17)$$

$$K_e' = \frac{\partial I_d}{\partial V_e} = \frac{\left(\frac{nV_{in}^2}{2L_m \cdot \left[V_{in} + n(V_o + V_F) + \frac{TR \cdot n(V_o + V_F)}{t_{ON}} \right]} \right)}{\left(1 - \frac{V_e}{V_{gd}} \frac{R_{d1} + R_{d2}}{R_{d2}} \right)} \cdot \left(\frac{R_{s1} C_{s1}}{V_{gd} R_{d2}} \right) \quad (18)$$

$$K_o' = \frac{\partial I_d}{\partial V_o} = \frac{-n^2 V_{in}^2 \left(1 + \frac{TR}{t_{ON}} \right)}{2L_m \left[V_{in} + n(V_o + V_F) + \frac{TR \cdot n(V_o + V_F)}{t_{ON}} \right]^2 t_{ON}} \quad (19)$$

$$K_{in}' = \frac{\partial I_d}{\partial V_{in}} = \frac{nV_{in}^2 + 2n^2 V_{in} V_o + \frac{2n^2 V_{in} V_o \cdot TR}{t_{ON}}}{2L_m \left[V_{in} + n(V_o + V_F) + \frac{TR \cdot n(V_o + V_F)}{t_{ON}} \right]^2 t_{ON}} \quad (20)$$

It shows that the current \hat{I}_d is not related to \hat{I}_a , but a function of \hat{V}_o , \hat{V}_{in} and \hat{V}_e in equation (17). So the output current is completely decoupled from the auxiliary load and also has the capability against V_o and V_{in} transients.

Similarly, the transfer function from error voltage \hat{V}_e to output current \hat{I}_o is obtained in equation (21).

$$G_{ie} = \left. \frac{\hat{I}_o}{\hat{V}_e} \right|_{\hat{V}_{in}=0} = \frac{Z \cdot K_e'}{R_{dyn} \cdot (1 - Z \cdot K_o')} \quad (21)$$

It is noticed that by using the proposed control scheme, when the Flyback stage is operating at $V_{LEDmin}=20V$, the DC gain is reduced and getting closer to the case of $V_{LEDmax}=60V$ (shown in Figure 17). At minimum current condition, the DC gain is also reduced to make the system easier to control for system stability.

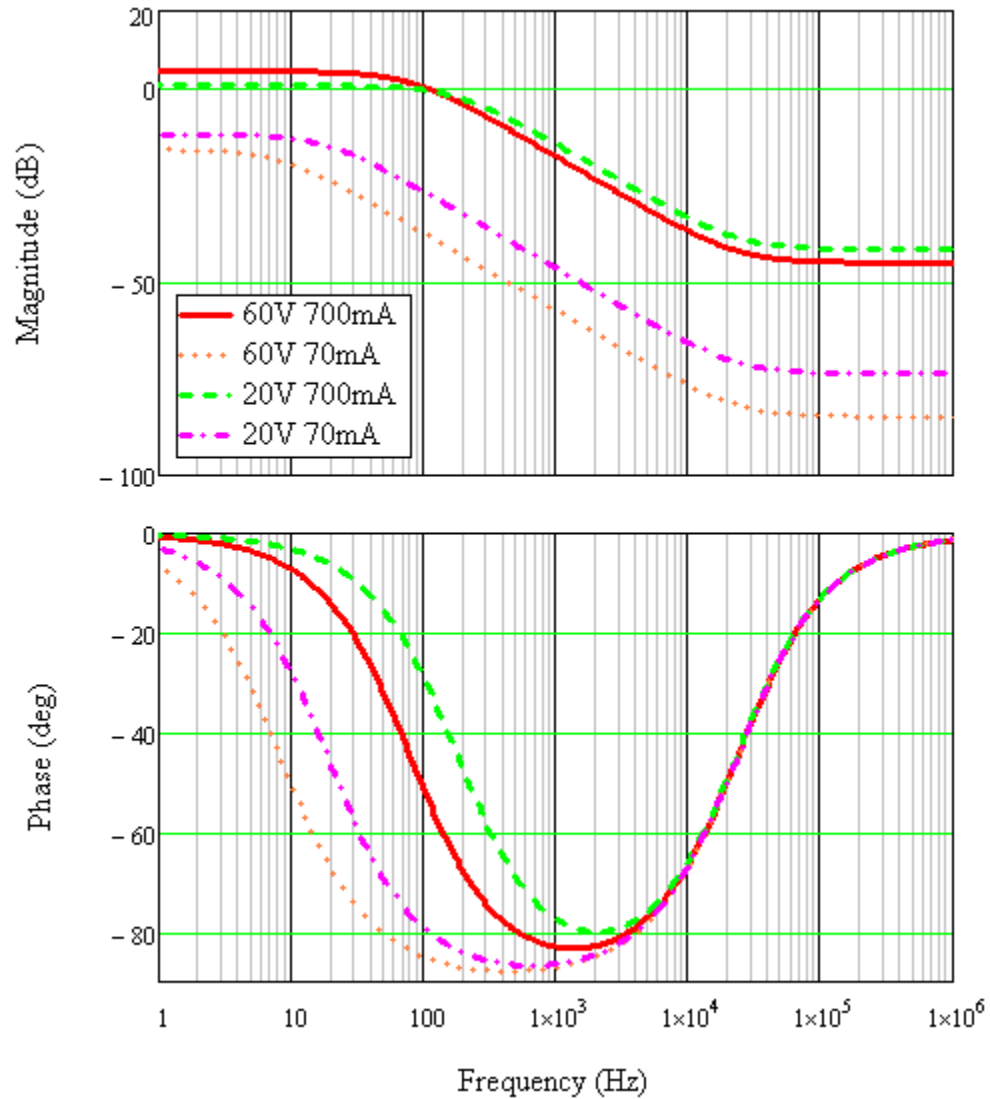


Figure 17 Bode plot of G_{ie} for proposed control scheme

VI. EXPERIMENTAL VERIFICATION

The design parameters of the prototype used in the experiments are shown in Table 2.

Table 2 Design Parameters in the experimental prototype

Design Parameter	Design Value or Description
V_{in}	425Vdc (min)
V_{omin}	20Vdc
V_{omax}	60Vdc
I_{omin}	70mA
I_{omax}	700mA
L_m	3.0mH EE 25/16/9 core
L_k	Leakage inductance, 25 μ H (max)
n	122:30
n_a	122:6
QI	STF5N95K3 FET N 950V 3.5 Ohm TO-220FP
DI	2x ES2G in parallel Diode, 400V, 2A, SMB
R_{sI}	5.1k Ω
C_{sI}	470pF
R_{dI}	10k Ω
R_{d2}	1.5k Ω
R_{sense}	2.7 Ω //2.7 Ω
LED Load	LUMILEDS LUXEON Rebel ES
Auxiliary Load	1.8W Fan Load+1.2W Resistive Load

In Figure 18, at full output power, the V_{ramp} signal peak shown in CH2 (green) is close to 1.3V and the maximum t_{ON} is about 4.5 μ s and the maximum power 40W can be achieved. This is very similar to the simulation in Figure 9 and calculated results in Figure 11 and Figure 13. Compared

with the real current sensing signal in CH3 (pink), V_{ramp} clearly shows a saturated nonlinear top. In the experiment, a fan load (1.8W output power) is used as a worst case load with DC+AC current demand. The fan's vibrator is working during the higher half of the cycle, resulting in noisy current waveform in Figure 18 CH1 (Yellow).



Figure 18 Experimental results at full load (CH1-Yellow: Fan current; CH2-Green: V_{ramp} ; CH3-Pink: I_{Q1} ; CH4-Blue: V_{ds} of Q1)

In Figure 19, LED output power $P_{out}=1.4W$ (3.5% of P_{max}), the V_{ramp} signal peak is close to 200mV and the minimum t_{ON} is about 500ns. This is very similar to the simulation in Figure 9 and calculated results in Figure 11 and Figure 13. The minimum power can be reached with the same fan load running at the same time. From the zoom-in figure on the bottom, a stable switching is observed; even the FET current sensing signal (CH3: Pink) is distorted by the fan load.

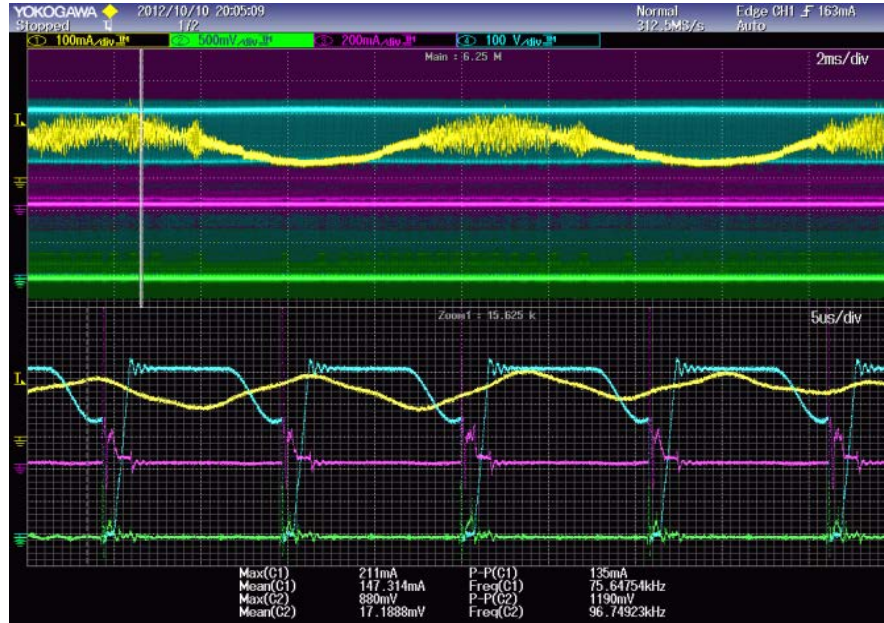


Figure 19 Experimental results at light load (CH1-Yellow: Fan current; CH2-Green: V_{ramp} ; CH3-Pink: I_{Q1} ; CH4-Blue: V_{ds} of Q1)

A MOSFET is used to switch the auxiliary load on and off with gate control signal in the following auxiliary load transient tests. The load consists of a resistive load and a cooling fan load. The additional resistive load is to increase the loading transient step and the slew rate, due to the slow ramping up of the fan load.

In Figure 20, AUX load transient test is conducted at 0.1Hz switching. The CH1 (Yellow) signal is the load control switch voltage (drain to source), so during loading on the auxiliary supply, the switch is closed and zero voltage is across drain to source. While during the unloading step, the switch is off and about 12Vdc is across the drain to source. From the zoom-in figure, it demonstrates a flat and non-interrupted output current in CH2 (Green) at 20V minimum LED voltage and 70mA driving current (10% dimming).

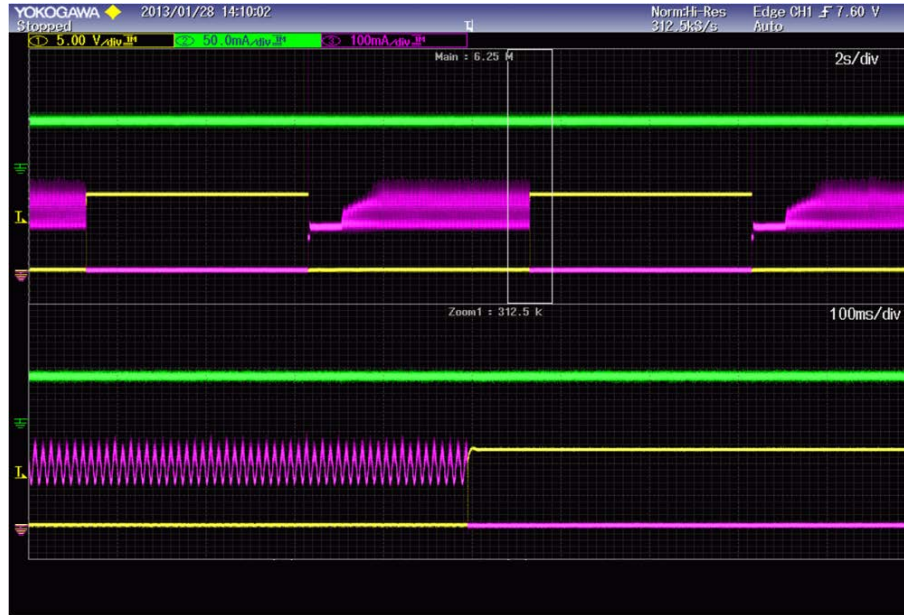


Figure 20 Transient performance during AUX load changes at 0.1Hz (CH1-Yellow: Control switch voltage of the auxiliary load, CH2-Green: Load current at 70mA, CH3-Pink: Auxiliary load current, 1.2W resistive load+1.8W fan load)

In Figure 21, 1kHz AUX load transient test is conducted and in this case, the fan load is inactive. The CH1 (Yellow) signal is again the load control switch voltage (drain to source), so during loading step, the switch is closed and zero voltage is across drain to source. While during the unloading step, the switch is off and about 12Vdc is across the drain to source. From the zoom-in figure, it demonstrates a flat and non-interrupted output current in CH2 (Green) at 20V minimum LED voltage and 70mA driving current (10% dimming).



Figure 21 Transient performance during AUX load changes at 1kHz (CH1-Yellow: Control switch voltage of the auxiliary load, CH2-Green: Load current at 70mA, CH3-Pink: Auxiliary load current, 1.2W resistive load+1.8W fan load)

The comparative Bode plots of G_{ie} are shown in Figure 22 for the proposed scheme using mathematical model and experimental measurements. It demonstrates that the presented small signal model is very accurate up to several kHz, where the system cross over frequency will locate. And beyond 10kHz, the small signal model based on the average value of each switching cycle starts to deviate from the measurement [45]. The system can be designed to be less sensitive for V_o change and the system DC gain is reduced at lower V_o . ($V_{LEDmax}=60V$, $I_{LEDmax}=700mA$, $V_{LEDmin}=20V$, $I_{LEDmin}=70mA$).

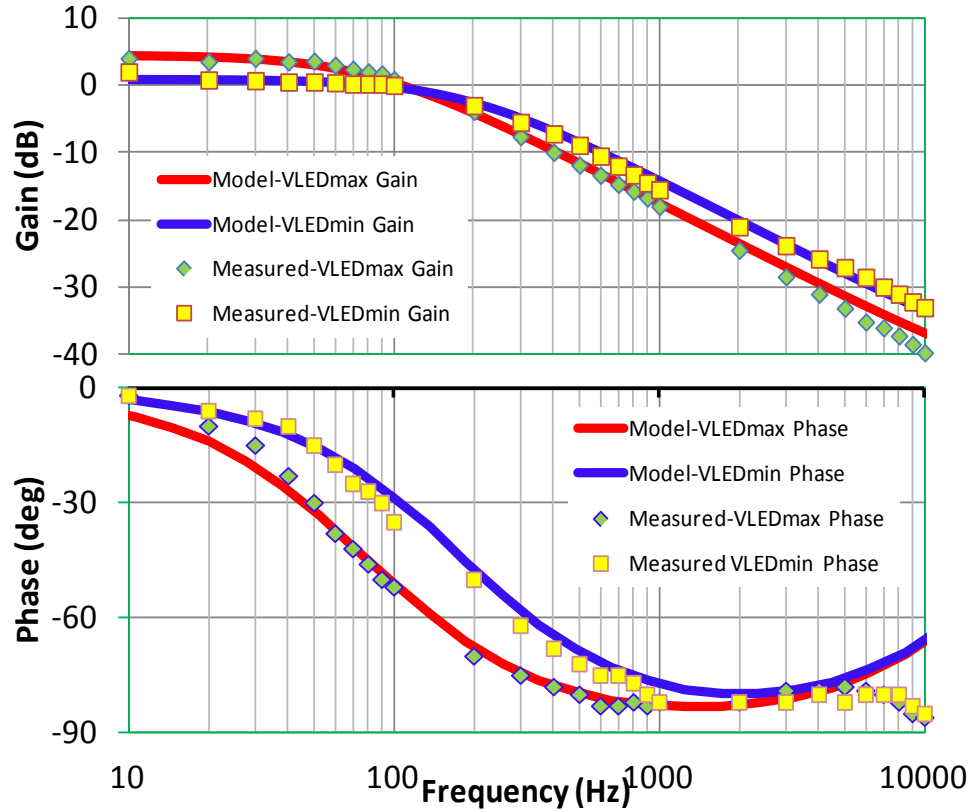


Figure 22 Bode plot of G_{ie} for proposed control scheme, mathematical model VS measurements

A typical 0-10V dimmer circuit is shown in Figure 23. VR_{mk7} , $R_{mk7}2$, C_{mk7} and Q_{mk7} form an adjustable voltage source. The voltage between base and emitter, V_{be} is used in this case as the reference voltage at about 0.6V and the voltage between violet and grey leads can be calculated in (22). Z_{mk7} is for over voltage protection when the user misconnects the dimmer to high voltages, such as AC mains.

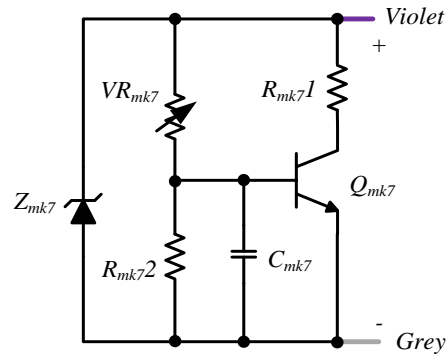


Figure 23 A Simple 0-10V/Mark 7 dimmer

$$V_{\text{dim}} \approx \frac{V_{be-Qmk7}}{R_{mk7} \cdot 2} \cdot (VR_{mk7} + R_{mk7} \cdot 2) \quad (22)$$

The ballast/driver will read the voltage different between violet and grey leads V_{dim} and control the light output. In Figure 24, the dimming curves are measured with the prototype at different case temperatures of -20, 25 and 70 °C and AUX fan loading. A standardized 0-10V dimming controller is used in the experiment and the driver outputs 100% when the dimming voltage is larger than 8V and 10% when the dimming voltage is lower than 1V [3]. It demonstrates that the proposed topology and control scheme provide very stable and accurate output driving current with wide dimming range and temperature variations.

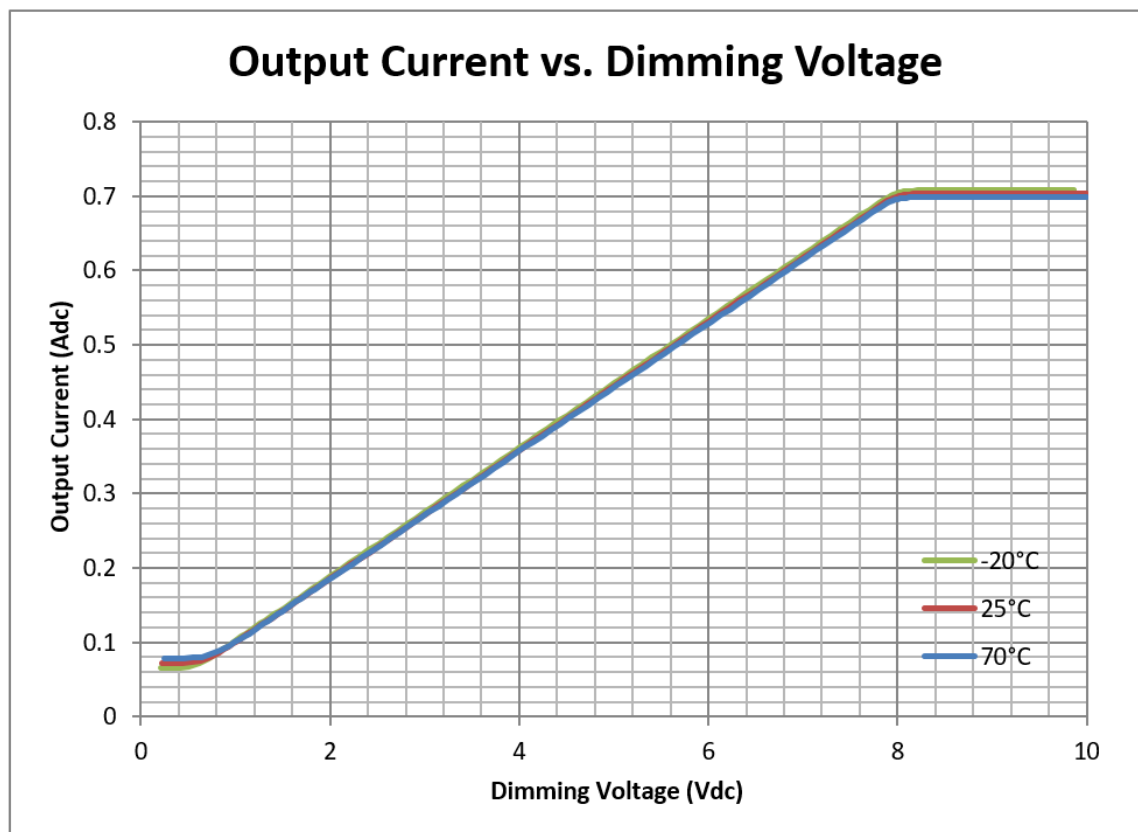


Figure 24 Experimental dimming performance with AUX loading at different operating temperatures

The measured efficiency of the Flyback stage with and without auxiliary loading is shown in Figure 25. 1.8W fan is used for the loading during efficiency measurement. For more than 15W output LED load power, the driver output current is 700mA with different number of LEDs. And for below 15W output power, the driver efficiency is measured with output current dimming.

Without the auxiliary loading, the peak efficiency of the LED driver is $\sim 92.1\%$, and with the 1.8W auxiliary loading, the peak LED power efficiency is about 4.9% lower at $\sim 87.2\%$. It is worth noting that the 1.8W auxiliary loading (real power to the fan) is not included in the LED output power in the plot. So the efficiency drop, especially at low LED load power, is mainly due to this reason, and the actual total loss in the LED driver is not that much.

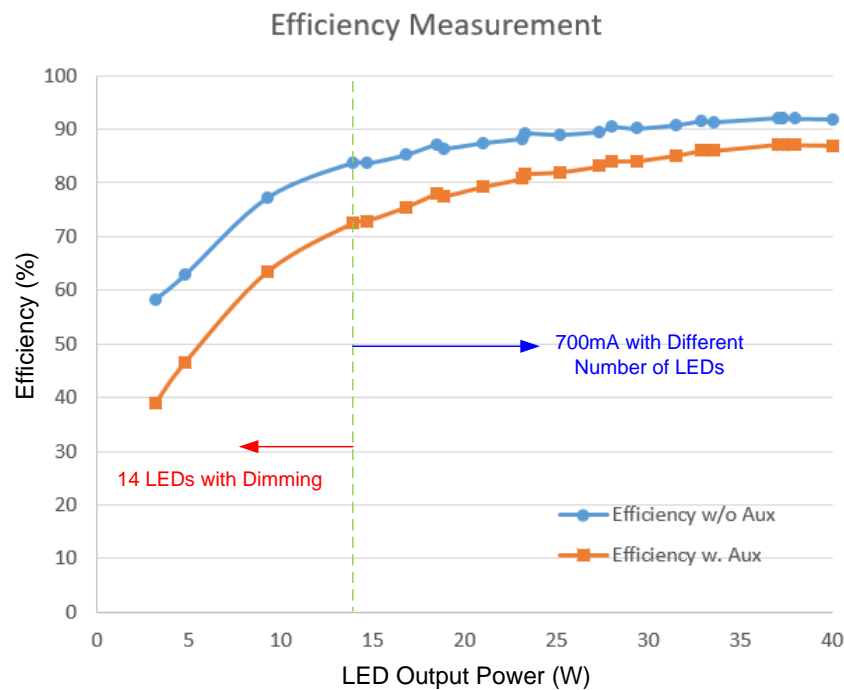


Figure 25 Measured efficiency output LED load power VS the overall input power with and without auxiliary loading (with 1.8W fan load)

VII. CONCLUSION

In this paper, a novel control scheme is introduced to regulate CC LED output and CV AUX output at the same time for a Flyback based LED driver architecture. Using a nonlinear ramp signal, the main CC output is decoupled from the CV auxiliary output, so that LED flickering issue at dimming condition is completely resolved. Advantages of the proposed method are explained by building the small signal model. Based on the provided design guidelines, simulations and experimental results are presented to verify the proposed control scheme. Finally, experiments under steady state and auxiliary load transient confirm the effectiveness of the control scheme in the 40W dimmable LED driver with a 12V 3W AUX supply.

APPENDIX

The derivation of critical equations in this paper will be shown in more details in this section.

A. Derivation of t_{ON} in Equation (2)

Equation (2) is derived from the power delivery from the inductance L_m in the Flyback converter, where I_{pk} is the peak current of L_m and f_{sw} is the switching frequency.

$$P_{in} = \frac{P_o}{\eta} = \frac{1}{2} \cdot L_m I_{pk}^2 f_{sw} = \frac{1}{2} \cdot L_m \left(\frac{V_{in}}{L_m} \cdot t_{ON} \right)^2 \frac{1}{t_{ON} + t_{dis} + TR} \quad (23)$$

t_{dis} is the discharging time of the magnetizing current, which can be calculated in (24). And TR is the quasi-resonant duration, which can be found in (25).

$$t_{dis} = \frac{V_{in}}{n(V_o + V_F)} t_{ON} \quad (24)$$

$$TR = \pi \sqrt{L_m C_{tot}} \quad (25)$$

Substitute (24) and (25) into (23), we can then obtain

$$\frac{1}{2} \cdot \frac{V_{in}^2}{L_m} \cdot t_{ON}^2 - \frac{P_o}{\eta} \left(\frac{V_{in}}{n(V_o + V_F)} + 1 \right) \cdot t_{ON} - \frac{P_o}{\eta} \left(\pi \sqrt{L_m C_{tot}} \right) = 0 \quad (26)$$

And the t_{ON} can be solved using equation (2) finally and only the positive solution will be taken.

B. Derivation of I_d in Equation (7)

Firstly, the current of the auxiliary load I_a is reflected to primary side when the main FET turns on and the average value of this current I_{ap} during on time can be found in (27) and geometry of the waveform is shown in Figure 26.

$$I_a = \frac{I_{ap} \cdot t_{ON} \cdot n_a}{t_{ON} + t_{OFF}} \Leftrightarrow I_{ap} = \frac{I_a (t_{ON} + t_{OFF})}{t_{ON} \cdot n_a} \quad (27)$$

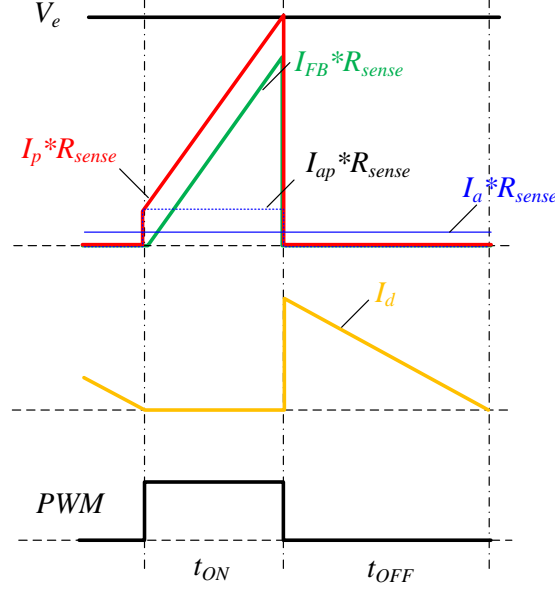


Figure 26 Waveform for derivation of (7)

To calculate the average current I_d , we can use (28) to obtain the peak of the I_{FB} , I_{FB_pk} in Figure 26 and then reflect this value to secondary side and average it over the switching period in (29).

$$I_{FB_pk} = \frac{V_e}{R_{sense}} - I_{ap} = \frac{V_e}{R_{sense}} - \frac{I_a (t_{ON} + t_{OFF})}{t_{ON} \cdot n_a} \quad (28)$$

$$I_d = \frac{I_{FB_pk} \cdot n \cdot t_{OFF}}{2(t_{ON} + t_{OFF})} = \frac{\left(\frac{V_e}{R_{sense}} - I_{ap} \right) \cdot n \cdot t_{OFF}}{2(t_{ON} + t_{OFF})} \quad (29)$$

Finally, we can substitute (27) into (29) and in order to simplify the equation in an explicit form without losing the insight of the coupling between I_a and I_d , we assume in the (29), $t_{OFF} = t_{dis}$. However, in the Figure 16, we still consider the time duration TR , which is the difference between t_{OFF} and t_{dis} .

C. Derivation of I_d in Equation (16)

Using the nonlinear ramp proposed in this paper, the t_{ON} can be derived from (30).

$$V_e = V_{gd} \left(1 - e^{-\frac{t_{ON}}{R_{s1}C_{s1}}} \right) \frac{R_{d2}}{R_{d1} + R_{d2}} \quad (30)$$

Similar to the derivation of equation (7), we can obtain the peak of the I_{FB} , I_{FB_pk} on the primary side and calculate the average value of I_d over a switching cycle on the secondary side as in (31).

$$I_d = \frac{I_{FB_pk} \cdot n \cdot t_{dis}}{2(t_{ON} + t_{OFF})} = \frac{\left(\frac{V_{in}}{L_m} \cdot t_{ON} \right) \cdot n \cdot t_{dis}}{2(t_{ON} + t_{dis} + TR)} \quad (31)$$

Substitute (24) and (25) into (31), we can obtain the equation (16).

REFERENCES

- [1] L. Jia, D. Fang and Y. F. Liu, "Control Scheme for Decoupling Auxiliary Power Supply in Dimmable LED Drivers", in Proc. IEEE Energy Conversion Congress and Exposition (ECCE), 2014, pp.5257-5264
- [2] J. Weinert, "LED Lighting Explained", Philips, 2013
- [3] Philips, "Xitanium LED ELECTRONIC DRIVERS", 2015
- [4] OSRAM, "Technical application guide OPTOTRONIC® LED drivers for indoor application", Sept. 2015
- [5] Silvair, "Introduction to Smart Lighting, 2015,
https://www.silvair.com/assets/contents/media/Introduction_to_SMART_LIGHTING.pdf
- [6] Cree, "2014 LED Lighting Catalog", 2014,
<https://www.creelink.com/exLink.asp?6333393OQ74M87I30973573>
- [7] Philips Lumileds, "Philips Lumileds Illumination Grade Portfolio", 2014,
<http://www.philipslumileds.com/uploads/418/BR10-pdf>
- [8] LUXEON Rebel ES high brightness white power LED, datasheet available online:
<http://www.philipslumileds.com/pdfs/DS61.pdf>
- [9] LUXEON M High Flux Density and Efficacy LED, datasheet available online:
www.philipslumileds.com/uploads/354/DS103-pdf
- [10] R. A. Pinto, M. R. Cosetin, A. Campos, M. A. Dalla Costa, and R. N. do Prado, "Compact emergency lamp using power LEDs," IEEE Trans. Ind. Electron., vol. 59, no. 4, pp. 1728–1738, Apr. 2012.
- [11] H. J. Chiu, Y. K. Lo, J. T. Chen, S. J. Cheng, C. Y. Lin, and S. C. Mou, "A high-efficiency dimmable LED driver for low-power lighting applications," IEEE Trans. Ind. Electron., vol. 57, no. 2, pp. 735–743, Feb. 2010.
- [12] D. Gacio, J. M. Alonso, J. Garcia, L. Campa, M. J. Crespo, and M. Rico-Secades, "PWM series dimming for slow-dynamics HPF LED drivers: The high-frequency approach," IEEE Trans. Ind. Electron., vol. 59, no. 4, pp. 1717–1727, Apr. 2012.
- [13] "Improving System Reliability with SynJet® Cooling", available online:
https://www.imaps.org/chapters/centraltexas/Symposium_Presentations/Improving%20System%20Reliability%20with%20SynJet%20Cooling.pdf
- [14] "SynJet® Thermal Management Technology Increases LED Lighting System", available online: <http://paris.utdallas.edu/IEEE-RS-ATR/document/2009/2009-12.pdf>
- [15] L. Chies, M. F. de Melo, W. D. Vizzotto, R. Spannemberg, V. C. Bender and M. A. Dalla Costa, "Design space for LED systems considering photoelectrothermal aspects," 2016 IEEE Industry Applications Society Annual Meeting, Portland, OR, 2016, pp. 1-8.

- [16] “Low Noise, High Reliability Cooling for HBLEDs”, available online: <http://www.em.avnet.com/en-us/design/marketsolutions/Documents/Lighting/LightSpeed-Eskow-0508.pdf>
- [17] Y-C Li; C-L Chen, "A Novel Primary-Side Regulation Scheme for Single-Stage High-Power-Factor AC–DC LED Driving Circuit", IEEE Trans on Industrial Electronics, Vol 60, Issue 11, 2013, pp 4978-4986
- [18] H. L. Cheng, Y. C. Hsieh, and C. S. Lin, “A novel single-stage high-power factor AC/DC converter featuring high circuit efficiency,” IEEE Trans. Ind. Electron., vol. 58, no. 2, pp. 524–532, Feb. 2011.
- [19] Y. C. Li and C. L. Chen, “A novel single-stage high-power-factor AC–DC LED driving circuit with leakage inductance energy recycling,” IEEE Trans. Ind. Electron., vol. 59, no. 2, pp. 793–802, Feb. 2012.
- [20] D. Gacio, J. M. Alonso, A. J. Calleja, J. García, and M. R.-Secades, “A universal-input single-stage high-power-factor power supply for HB-LEDs based on integrated buck–flyback converter,” IEEE Trans. Ind. Electron., vol. 58, no. 2, pp. 589–599, Feb. 2011.
- [21] J. M. Alonso, J. Vina, D. Gacio, G. Martinez, and R. O. Sanchez, “Analysis and design of the integrated double buck–boost converter as a high power-factor driver for power-LED lamps,” IEEE Trans. Ind. Electron., vol. 59, no. 4, pp. 1689–1697, Apr. 2012.
- [22] C. S. Moo, K. H. Lee, H. L. Cheng, and W. M. Chen, “A single stage high-power-factor electronic ballast with ZVS buck–boost conversion,” IEEE Trans. Ind. Electron., vol. 56, no. 4, pp. 1136–1146, Apr. 2009.
- [23] H. S. Athab, D. D. Lu, and K. Ramar, “A single-switch AC/DC flyback converter using a CCM/DCM quasi-active power factor correction front-end,” IEEE Trans. Ind. Electron., vol. 59, no. 3, pp. 1517–1526, Mar. 2012.
- [24] P. Fang, Y.F. Liu and P. C. Sen, "A Flicker-Free Single-Stage Offline LED Driver With High Power Factor," IEEE Journal of Emerging and Selected Topics in Power Electronics, September.2015, pp.654-665.
- [25] B. White, H. Wang, Y.F. Liu and X. Liu, "An Average Current Modulation Method for Single-Stage LED Drivers With High Power Factor and Zero Low-Frequency Current Ripple," IEEE Journal of Emerging and Selected Topics in Power Electronics, September.2015, pp.714-731.
- [26] Y. Qiu, L. Wang, H. Wang, Y.F. Liu and P. C. Sen, "Bipolar Ripple Cancellation Method to Achieve Single-Stage Electrolytic-Capacitor-Less High-Power LED Driver," IEEE Journal of Emerging and Selected Topics in Power Electronics, September. 2015, pp.698-703.
- [27] D. Camponogara, D. Ribeiro Vargas, M. A. Dalla Costa, J. M. Alonso, J. Garcia, and T. Marchesan, “Capacitance reduction with an optimized converter connection applied to LED drivers,” IEEE Trans. Ind. Electron., vol. 62, no. 1, pp. 184–192, Jan. 2015.

- [28] VIPER16, “Fixed frequency VIPer™ plus family”, datasheet available: <http://www.st.com/web/en/resource/technical/document/datasheet/CD00218828.pdf>
- [29] P. Antoszczuk, R. G. Retegui and G. Uicich, "Interleaved Boundary Conduction Mode Versus Continuous Conduction Mode Magnetic Volume Comparison in Power Converters," in IEEE Transactions on Power Electronics, vol. 31, no. 12, pp. 8037-8041, Dec. 2016.
- [30] C. BASSO, AN1681/D, Application Notes, ON semiconductor, “How to Keep a FLYBACK Switch Mode Supply Stable with a Critical-Mode Controller”, Sept. 2000
- [31] ST 5970D, “Up to 1A step Down Switching Regulator”, datasheet available online: http://www.st.com/web/catalog/sense_power/FM142/CL1456/SC355/PF63222
- [32] UL1310, “Standard for Class 2 Power Units”, available online: <http://ulstandards.ul.com/standard/?id=1310>
- [33] B. T. Irving, Y. Panov, and M. Jovanovic, “Small-signal model of variable frequency flyback converter”, IEEE Applied Power Electronics Conf. (APEC) Proc., pp.997-982, March 2003.
- [34] R.B. Ridley, “A new continuous-time model for current-mode control with constant frequency, constant on-time, and constant off-time, in CCM and DCM”, IEEE Power Electronics Specialists Conf. (PESC) Rec., pp.382-389, June 1990.
- [35] V. Vorperian, “Simplified analysis of PWM converters using the model of the PWM switch part II: discontinuous conduction mode”, Virginia Power Electronics Center (VPEC) Seminar Proc., pp.10-20, Sept. 1989.
- [36] J. Lempinen and T. Suntio, “Small-signal modeling for design of robust variable-frequency flyback battery chargers for portable device applications”, IEEE Applied Power Electronics Conf. (APEC) Proc., pp.548-554, March 2001.
- [37] J. Chen, R. Erickson, and D. Maksimović, “Averaged switch modeling of boundary conduction mode dc-to-dc converters”, IEEE Industrial Electronics Society Conf. (IECON), pp.844-849, Nov. 2001.
- [38] D.M. Mitchell, “Tricks of the trade: understanding the right-half-plane zero in small-signal dc-dc converter models”, IEEE Power Electronics Society Newsletter, pp.5-6, January 2001.
- [39] B.T. Irving and M.M. Jovanović, “Analysis and design of self-oscillating flyback converter”, IEEE Applied Power Electronics Conf. (APEC) Proc., pp.897-903, March 2002.
- [40] Y. Panov and M. Jovanovic, “Performance evaluation of 70-W two-stage adapters for notebook computers,” in Proc. IEEE APEC’99, 1999, pp.1059–1065.
- [41] Y. Panov and M. Jovanovic, “Adaptive off-time control for variable-frequency, soft-switched flyback converter at light loads,” in Proc. IEEE APEC’99, 1999, pp.457–462.
- [42] R. D. Middlebrook and S. Cuk, “A general unified approach to modeling switching-converter power stages,” Int. J. Electron., vol. 42, no. 6, pp. 521–550, 1977.

- [43] G. Spiazzi, D. Tagliavia, and S. Spampinato, “DC-DC flyback converters in the critical conduction mode: A re-examination,” in Proc. IEEE IAS’00, 2000, pp. 2426–2432.
- [44] T. Suntio, J. Lempinen, K. Hynynen, and P. Silventoinen, “Analysis and small-signal modeling of self-oscillating converters with applied delay,” in Proc. IEEE APEC’02, 2002, pp. 395–401.
- [45] R. Erickson, and D. Maksimović, “Fundamentals of Power Electronics”, Springer, 2nd edition, Jan 2001